

## Electron cooling behavior in cascading semiconductor double-quantum-well structures


Xiangyu Zhu<sup>1,\*</sup>, Chloé Salhani,<sup>1,2</sup> Guéric Etesse,<sup>3</sup> Naomi Nagai,<sup>1</sup> Marc Bescond,<sup>2,3,†</sup> Francesca Carosella,<sup>4</sup> Robson Ferreira,<sup>4</sup> Gérald Bastard<sup>4</sup> and Kazuhiko Hirakawa<sup>1,2,‡</sup>

<sup>1</sup>*Institute of Industrial Science, University of Tokyo, 4-6-1 Komaba, Meguro-ku, Tokyo 153-8505, Japan*

<sup>2</sup>*LIMMS-CNRS, IRL 2820, 4-6-1 Komaba, Meguro-ku, Tokyo 153-8505, Japan*

<sup>3</sup>*Faculté des Sciences de Saint Jérôme, IM2NP, UMR CNRS 7334, Aix-Marseille Université, Case 142, 13397 Marseille Cedex 20, France*

<sup>4</sup>*Physics Department, ENS-PSL, 24 rue Lhomond, F75005 Paris, France*

 (Received 1 February 2024; revised 13 June 2024; accepted 19 August 2024; published 5 September 2024)

We investigate evaporative electron cooling in cascading semiconductor double-quantum-well (QW) structures. In this cascading double QW structure (QW1 and QW2, where QW2 is on the anode side), one electron absorbs two longitudinal optical (LO) phonons as it travels from the cathode to the anode, for which efficient thermionic cooling is expected. By analyzing the high-energy tail of the photoluminescence spectra, the electron temperature in each QW is determined. When  $\text{Al}_{0.35}\text{Ga}_{0.65}\text{As}$  barriers are used, anomalous electron heating in QW2 due to hot electron distribution above the barrier is observed. By introducing taller barriers ( $\text{Al}_{0.7}\text{Ga}_{0.3}\text{As}$ ) before QW2 to suppress hot electron distribution above the barrier, electron cooling in both QWs by several tens of kelvins is achieved. Furthermore, oscillatory anticorrelated electron temperature change in the two QWs that results from LO-phonon scattering is observed.

DOI: [10.1103/PhysRevApplied.22.034012](https://doi.org/10.1103/PhysRevApplied.22.034012)

### I. INTRODUCTION

Progress in ultrahigh-density, ultrahigh-speed electronic and photonic devices has continually moved forward but at the expense of a tremendous generation of heat that results from the thermalization of hot carriers generated by high electric fields. Efficient cooling technologies are, therefore, needed for the continuous development of high-performance devices. So far, the thermoelectric Peltier effect has been most commonly used in solid-state coolers [1–3]. However, the cooling efficiency deteriorates due to scattering-induced internal Joule heating. Recently, thermionic cooling, which is based on the thermionic emission process, has been attracting considerable attention as potential solid-state coolers due to its expected high cooling efficiency [4–9]. In such a case, above an energy barrier from a cathode to an anode, hot electrons are thermionically extracted. As a result, no degradation in cooling efficiency due to scattering-induced Joule heating exists [10].

To achieve high cooling efficiency, Chao *et al.* proposed a thermionic cooling structure with asymmetric double

barriers [11] [hereafter, we call this the “asymmetric double barrier (ADB) thermionic cooler”]. In the ADB structure, a quantum well (QW) is sandwiched between two potential barriers. Energy-filtered electrons are injected by resonant tunneling from the emitter electrode to a quantized state in the QW through the thin and tall barrier on the emitter side. Then, electrons injected into the QW are extracted by thermionic emission above the second (thick and low) barrier [11]. By using this sequential transport process, significant electron cooling (up to 30 K) can be achieved at room temperature [12,13]. However, in the ADB structure, one injected electron typically absorbs only one longitudinal optical (LO) phonon [14–16].

Inspired by the concept of the quantum cascade lasers, in which one electron emits multiple photons as it travels through many stages of cascading QW structures, we have designed a structure in such a way that one electron absorbs multiple LO phonons in the sequential cascading transport process. This process is expected to enhance the lattice cooling efficiency compared with that in ADB structures. In this work, we have investigated electron transport and electron cooling behavior in cascading double QW structures [hereafter, we call this structure the quantum cascade cooling (QCC) structure]. Although we want to discuss lattice cooling effects in the QCC structure, the determination of lattice temperatures in nanometer-thick films is

\*Contact author: [zxy@iis.u-tokyo.ac.jp](mailto:zxy@iis.u-tokyo.ac.jp)

†Contact author: [bescond@iis.u-tokyo.ac.jp](mailto:bescond@iis.u-tokyo.ac.jp)

‡Contact author: [hirakawa@iis.u-tokyo.ac.jp](mailto:hirakawa@iis.u-tokyo.ac.jp)

extremely challenging since there is no suitable method for measuring local lattice temperatures sensitively. Furthermore, the expected lattice cooling in our structure is only in the order of a few microkelvins [14–16]. Therefore, in the present work, we focus our attention on the electron temperature in the QCC structure to understand electron transport and cooling physics in the QCC. When a uniform barrier height is used for the QCC structure, anomalous electron heating is observed in the downstream QW. This is identified to be due to the hot electron population above the barrier, which originates from direct thermionic emission from the electrode and the upstream QW. When the injection barriers are made taller to block the hot electron population, we observe electron cooling in both QWs. Furthermore, an anticorrelated oscillation in the electron temperatures in the QWs is seen, which is due to the competition between LO-phonon-assisted sequential transport and quasielastic scattering processes. Evaporative electron cooling by as much as 70 K is also observed.

## II. EXPERIMENT

The QCC samples were grown on n-type GaAs (100) substrates by using molecular beam epitaxy. We successively grew a 300-nm-thick n-GaAs emitter layer (Si doping density =  $1 \times 10^{17} \text{ cm}^{-3}$ ), an undoped 6-nm-thick  $\text{Al}_{0.35}\text{Ga}_{0.65}\text{As}$  emitter barrier, an undoped 5-nm-thick  $\text{Al}_{0.1}\text{Ga}_{0.9}\text{As}$  QW (QW1), an undoped 6-nm-thick  $\text{Al}_{0.35}\text{Ga}_{0.65}\text{As}$  barrier, an undoped 5-nm-thick  $\text{Al}_{0.2}\text{Ga}_{0.8}\text{As}$  QW (QW2), an undoped 30-nm-thick  $\text{Al}_{0.35}\text{Ga}_{0.65}\text{As}$  collector barrier, a 200-nm-thick n-GaAs collector layer (Si doping density =  $1 \times 10^{17} \text{ cm}^{-3}$ ), and a 10-nm-thick  $\text{n}^+\text{-GaAs}$  contact layer (Si doping density =  $5 \times 10^{18} \text{ cm}^{-3}$ ) [17–19]. The band diagram of the sample is schematically illustrated in Fig. 1(a) (referred to as QCC-A). The quantum wells are sandwiched between

$\text{Al}_{0.35}\text{Ga}_{0.65}\text{As}$  barriers. The energy separation between the two quantized states in QW1 (referred to as  $E_1$ ) and QW2 (referred to as  $E_2$ ) at zero bias voltage is around 70 meV. The wafer was patterned into mesa structures with various areas ranging from  $80 \times 80 \mu\text{m}^2$  to  $800 \times 800 \mu\text{m}^2$ . The AuGeNi/Au contacts were deposited on the front and back sides of the mesas, except for window areas, to perform optical characterization. The samples were annealed at  $450^\circ\text{C}$  in Ar ambient for 5 s. At the center of the mesas, a semitransparent NiCr layer was deposited as a window for photoluminescence measurements.

To clarify the level alignment as a function of the applied voltage,  $V$ , we measured the current–voltage ( $I$ - $V$ ) characteristics from 300 to 6 K. Figure 1(b) shows the  $I$ - $V$  curves measured at various temperatures,  $T$ . The  $I$ - $V$  curves near 300 K are rather featureless. As  $T$  is reduced below 100 K, the current flow is more dominated by the tunneling process. In particular, at  $T = 6$  K, steplike features are observed. Using the  $I$ - $V$  curve measured at  $T = 6$  K, we can discuss the level alignment in actual samples. If we assume a uniform electric field distribution between the emitter and collector electrodes, the resonance between  $E_1$  and  $E_2$  is expected at  $V \sim 0.3$  V. Since the current at 0.3 V is in the order of picoamperes, there is almost no influence of series resistances. The alignment between  $E_2$  and the conduction band edge in the emitter is expected at  $V \sim 0.55$  V. For  $V > 0.55$  V,  $E_2$  drops below the emitter conduction band, which leads to a small curvature change at  $V \sim 0.6$  V in Fig. 1(b). Similarly, the alignment between  $E_1$  and the conduction band edge occurs at  $V \sim 1$  V [see Fig. 3(b), which is obtained via the nonequilibrium Green’s function (NEGF) calculations that are discussed later]. Due to series resistance effects in the sample and in the measurement setup, the level alignment voltages at 300 K shift to the higher voltage side, which is discussed in the next section.

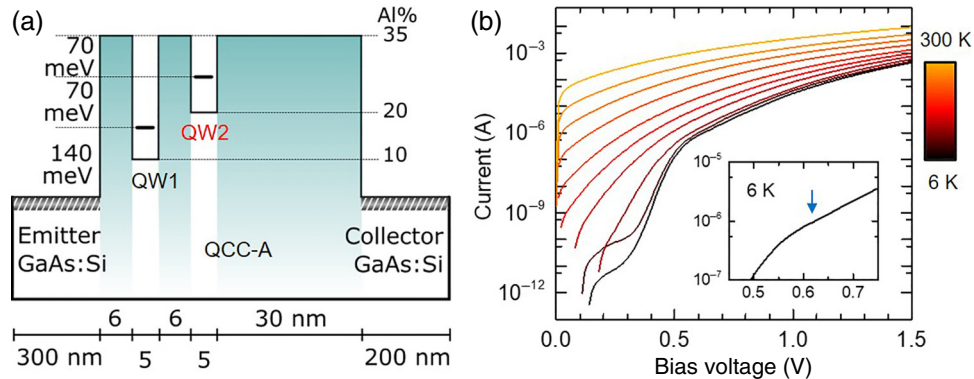


FIG. 1. (a) Band diagram of the cascading double AlGaAs/GaAs QW thermionic cooling heterostructure (QCC-A). Electrons are injected from the emitter electrode into the first QW through the first barrier by resonant tunneling. They are then injected from the first QW into the second QW through the second barrier by intersubband transition and are finally extracted to the collector by the thermionic emission above the third barrier. (b) Current  $I$  of QCC-A (using a log scale) measured as a function of bias voltage  $V$  at various temperatures from 6 to 300 K.

### III. DETERMINATION OF ELECTRON TEMPERATURES

Thermionic cooling devices are operated distant from equilibrium conditions. Therefore, the electron system and the lattice system may have different thermodynamic temperatures. In this section, we discuss the temperature of the electron system (the electron temperature,  $T_e$ ) in the QCC structures. Here,  $T_e$  is determined by the balance between the input power to and output power from an electron system, which is described as follows:

$$\left\langle \frac{dE}{dt} \right\rangle = \frac{\langle k_B T_e \rangle - \langle k_B T_L \rangle}{\tau_e} = \frac{P_{in}(\mu_{QW}) - P_{out}(\mu_{QW})}{n_{QW}}, \quad (1)$$

where  $\langle k_B T \rangle$  means the average energy of the electron system at temperature  $T$ , and  $T_e$  and  $T_L$  are the electron and lattice temperatures;  $P_{in}$  and  $P_{out}$  are the input power to and output power areal densities from the electron system, respectively. Moreover,  $k_B$  is the Boltzmann constant,  $\tau_e$

is the energy relaxation time,  $\mu_{QW}$  is the electrochemical potential, and  $n_{QW}$  is the electron areal density in the QW. In a steady state, the change in the electron temperature can be expressed as

$$\Delta T_e = T_e - T_L \propto \frac{P_{in}(\mu_{QW}) - P_{out}(\mu_{QW})}{n_{QW}} \tau_e. \quad (2)$$

To determine  $T_e$ , we measured the photoluminescence (PL) spectra for various  $V$  [13]. The PL was measured through the semitransparent NiCr window on the mesa structure. We used a blue laser at a wavelength of 488 nm for excitation, which has a short penetration depth in the GaAs electrode ( $\sim 80$  nm) [20,21]. The use of a short penetration depth is important to reduce the PL intensity from the electrodes with respect to the PL from the QWs. We then observed PL peaks from the collector and emitter electrodes and from QW1 and QW2. For more information, see Supplementary Information [22].

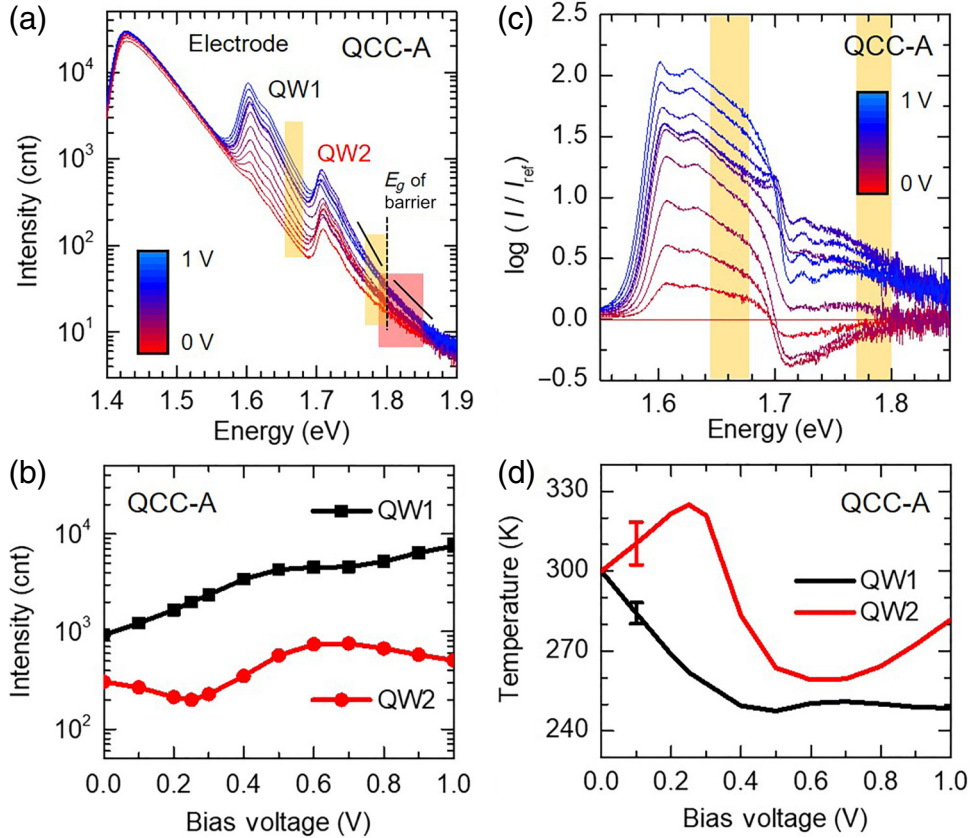


FIG. 2. (a) Photoluminescence (PL) spectra of QCC-A measured at 300 K for various bias voltages. The observed three PL peaks correspond to the recombination of electrons with holes in the electrode ( $\sim 1.43$  eV) and in the quantum wells (QW1  $\sim 1.6$  eV and QW2  $\sim 1.71$  eV). The energy ranges of the high-energy tail used for determining electron temperatures are highlighted in orange. The above-barrier hot electron PL is highlighted in red. (b) Intensity of the PL peak from QW1 (black) and QW2 (red) as a function of bias voltage. (c) Ratio between PL spectra measured for various  $V$  and the PL spectrum measured at  $V=0$  for determination of electron temperatures. The energy ranges of the high-energy tails are highlighted in orange. (d) Electron temperatures in QW1 (black) and QW2 (red) are plotted as a function of bias voltage.

Figure 2(a) plots the PL spectra of QCC-A measured for various  $V$  at 300 K [23]. There are three peaks in the spectra: (1) the peak at around 1.43 eV is the PL from the n-GaAs electrodes, (2) the peak at around 1.6 eV is the PL from QW1, and (3) the peak at around 1.71 eV is the PL from QW2. The intensity of the electrode PL does not change much when  $V$  is changed, whereas the PL intensities from QWs show a strong voltage dependence. In Fig. 2(b), we plot the peak intensities of the PL from QW1 (black) and QW2 (red) as a function of  $V$ . When  $V$  is increased from 0 to 0.3 V, the PL intensity of QW2 decreases with  $V$  and reaches a minimum at  $V \sim 0.25$  V. The QW2 PL then increases with  $V$  and arrives at a maximum at  $V \sim 0.6$  V. It starts decreasing for  $V > 0.6$  V since  $E_2$  drops below  $E_1$  and the resonant tunneling is shut off. On the other hand, the PL from QW1 increases with  $V$ , except for  $V \sim 0.6$  V, where resonant tunneling occurs.

In order to determine the electron temperatures,  $T_e$ , in QW1 and QW2, we first calculated the ratios between the PL spectra measured at  $V$  and the reference PL spectrum measured at  $V = 0$  and plotted them for various  $V$ , as shown in Fig. 2(c) [24]. The PL spectrum at  $V = 0$  represents the

thermal equilibrium emission at 300 K. The quantity  $T_e$  in QW1 and QW2 is calculated using the slope of the high-energy tail regions [highlighted in orange in Fig. 2(a)] and plotted as a function of  $V$  in Fig. 2(d). For the estimation of  $T_e$ , we assumed that the electron and hole temperatures are equal (for more detail, see Appendix A). Contrary to our expectation that electron cooling in QW2 could be observed owing to thermionic emission processes, we observed anomalous heating in QW2 as  $V$  was increased from 0 to 0.25 V. On the other hand, QW1 showed a significant cooling (by as much as 50 K).

#### IV. NONEQUILIBRIUM CURRENT FLOW CALCULATED BY THE NEGF

To clarify this unexpected electron heating behavior, we calculated the current density spectrum under a bias voltage by using the NEGF method [14–16]. Figure 3(a) shows the calculated current density spectrum when  $E_2 - E_1 = 36$  meV (the LO-phonon energy). As seen in this figure, not only the sequential tunneling current from QW1 to QW2 but also significant thermionic emission

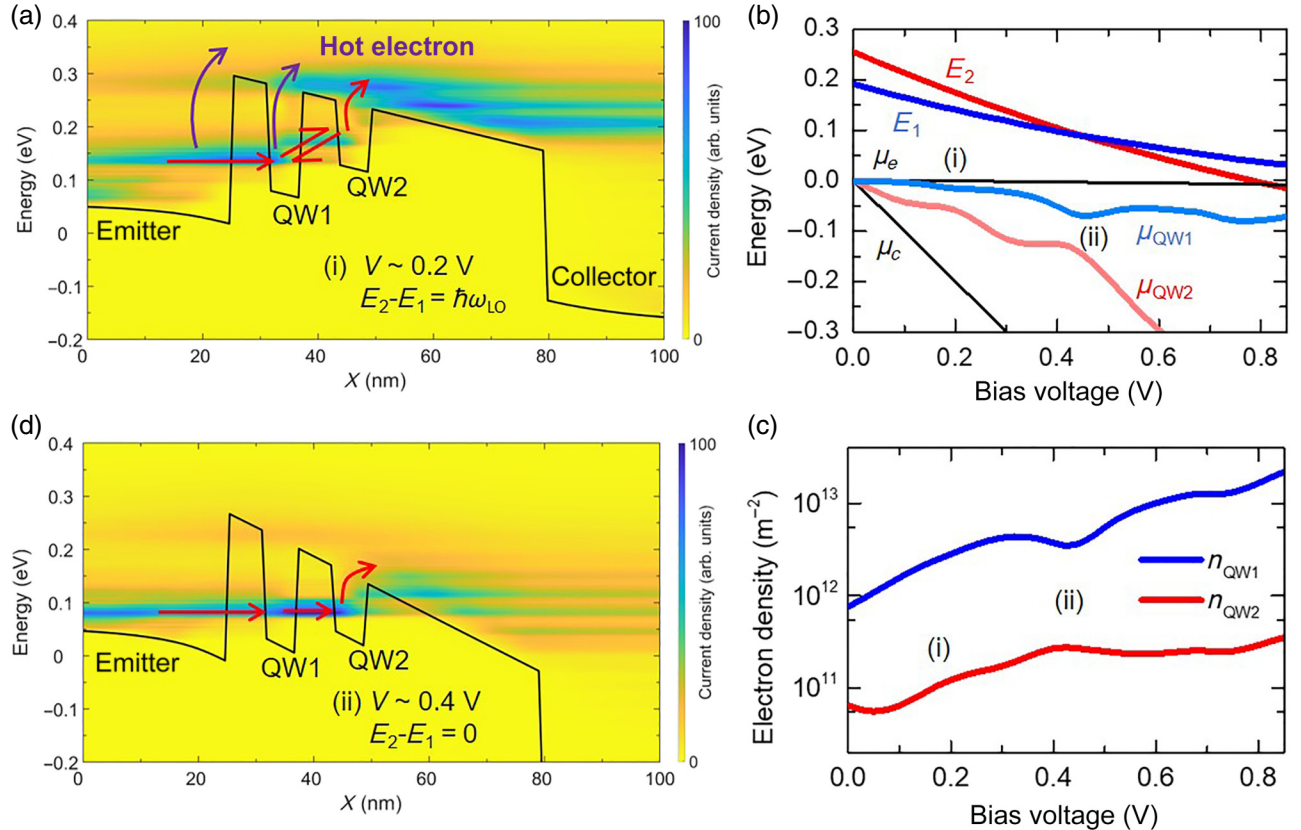


FIG. 3. (a) Current spectrum of the QCC-A structure when  $E_2 - E_1 = \hbar\omega_{LO}$  calculated using the nonequilibrium Green's function (NEGF) method. The current density is represented by a color bar. (b) Electrochemical potentials  $\mu_{QW1}$  (in QW1),  $\mu_{QW2}$  (in QW2),  $\mu_e$  (in the emitter), and  $\mu_c$  (in the collector) calculated as a function of  $V$  using the NEGF. The quantized states  $E_1$  (blue) and  $E_2$  (red) are also plotted. (c) Electron densities  $n_{QW1}$  (in QW1) and  $n_{QW2}$  (in QW2) calculated as a function of  $V$  using the NEGF. (d) Current spectrum of the QCC-A structure when  $E_2 - E_1 = 0$  (resonant tunneling condition).



current above the barrier is observed. Considering the current distribution of hot electrons, sequential transport from QW1 to QW2 is not efficient in QCC-A; there is direct thermionic emission from QW1 and from the emitter electrode to the states above the barrier. Indeed, we observe a clear slope difference below or above 1.8 eV in the PL spectra shown in Fig. 2(a) (note that the bandgap of  $\text{Al}_{0.35}\text{Ga}_{0.65}\text{As}$  is around 1.8 eV). Therefore, the anomalous electron heating in QW2 most likely originates from the interaction between electrons in QW2 and hot electrons above the barrier. From the NEGF calculations, the electron current density spectrum shown in Fig. 3(a) exhibits a significant above-barrier hot electron injection. The hot electron density above the barrier in the QW2 region has been estimated to be  $\sim 1.3 \times 10^{10} \text{ m}^{-2}$ , which is approximately 1/30 of the electron density in QW2 below the barrier. Considering the fact that the hot electrons are injected at much higher energies ( $\sim 100 \text{ meV}$  above the QW ground state), an increase in the electron temperature due to this high-energy electron cloud seems to be reasonable. A rough estimate using this density ratio and energy difference yields that the temperature of the electrons could be raised from 300 K to  $\sim 330 \text{ K}$ .

In Fig 3(b), the quantized subband energies,  $E_1$  and  $E_2$ , the electrochemical potentials,  $\mu_{\text{QW1}}$  and  $\mu_{\text{QW2}}$ , in QW1 and QW2, as well as the electrochemical potentials in the emitter and collector electrodes,  $\mu_e$  and  $\mu_c$ , are shown as a function of  $V$ . In this figure, we set the bottom of  $\mu_e$  at 0 eV. The energy difference between  $\mu_e$  and  $\mu_c$  is  $eV$ , where  $e$  is the elementary charge, and  $E_1$  and  $E_2$  decrease almost linearly with  $V$ . In contrast,  $\mu_{\text{QW1}}$  and  $\mu_{\text{QW2}}$  are strongly affected by electron injection and extraction resistances [13,25]. For example,  $\mu_{\text{QW2}}$  is determined

by the competition between the resistance of the tunnel injection from QW1 and the resistance of the thermionic emission to the collector. The resistance for electron injection from QW1 to QW2 decreases when  $E_2 - E_1$  becomes equal to the LO-phonon energy at  $V \sim 0.2 \text{ V}$  in Fig. 3(b) (LO-phonon-assisted tunneling). As a result, the  $\mu_{\text{QW2}}$  curve bends toward  $\mu_{\text{QW1}}$ . Similarly, another curve bending incident appears at the resonant tunneling condition ( $E_2 - E_1 = 0$ ) at  $V \sim 0.4 \text{ V}$  in Fig. 3(b). The electron concentrations in the two QWs,  $n_{\text{QW1}}$  and  $n_{\text{QW2}}$ , are calculated using the NEGF and plotted in Fig. 3(c). Although the characteristic voltage values are different between simulation and experiment due to the series resistance effect ( $\sim 50 \Omega$ ), the PL intensity shown in Fig. 2(b) shows a behavior very similar to the electron densities plotted in Fig. 3(c), indicating that the  $V$ -dependence of the PL intensities from the two QWs [shown in Fig. 2(b)] reflects the change in electron densities in the QWs. From a comparison between the PL intensities of QW1 and QW2 [see Fig. 2(b)] and the calculated  $n_{\text{QW1}}$  and  $n_{\text{QW2}}$  [see Fig. 3(c)], we argue that  $E_1 - E_2 = 0$  occurs at  $V \sim 0.6 \text{ V}$  and  $E_1 - E_2 = \hbar\omega_{\text{LO}}$  occurs at  $V \sim 0.3 \text{ V}$  in our actual QCC-A sample for PL measurements.

Note that, as seen in Fig. 2(d), electron heating due to the hot electron population above the barriers becomes most significant at  $V = 0.25 \text{ V}$ , where  $n_{\text{QW2}}$  becomes minimal and the effect of the above-barrier hot electron population on  $T_e$  becomes maximal, as expected from Eq. (2). At the resonant tunneling condition,  $n_{\text{QW1}}$  and  $n_{\text{QW2}}$  approach one another, as seen in Fig. 3(c). This resonant tunneling voltage is predicted at  $V \sim 0.4 \text{ V}$  using the NEGF, but it is shifted to  $\sim 0.6 \text{ V}$  in the experiment (see Fig. 2) [23]. Figure 3(d) plots the calculated current density spectrum

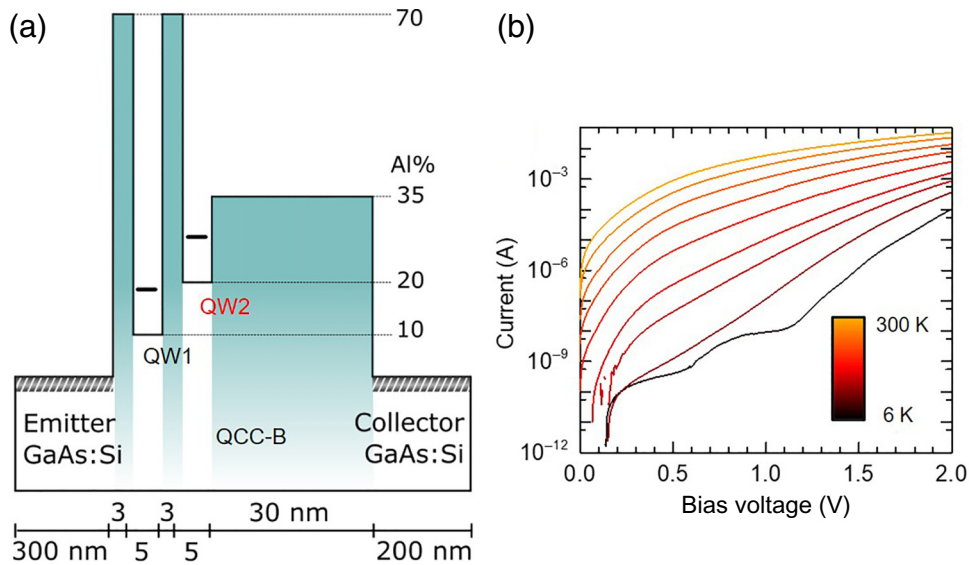


FIG. 4. (a) Band diagram of the cascading double AlGaAs/GaAs QW thermionic cooling heterostructure with tall barriers (QCC-B). (b) Current  $I$  of QCC-B (using a log scale) measured as a function of bias voltage  $V$  at various temperatures from 6 to 300 K.

at resonance. Under this condition, the above-barrier hot electron population disappears since the resonant tunneling provides a much less resistive transport channel to the electrons in QW1. Electrons injected into QW2 are extracted by the thermionic emission process and are cooled by evaporative cooling when  $0.3 \text{ V} < V < 0.6 \text{ V}$ . The quantity  $T_e$  in QW2 reaches a minimum at  $V \sim 0.6 \text{ V}$ , as shown in Fig. 2(d). For  $V > 0.6 \text{ V}$ ,  $E_2$  drops below  $E_1$  and  $T_e$  in QW2 increases again due to hot electron injection from QW1. By summarizing the experimental results on QCC-A, we can conclude that significant electron excitation to the above-barrier states induces anomalous electron heating in QW2, although the barrier height is as high as  $\sim 11k_B T$ .

## V. SUPPRESSING ABOVE-BARRIER ELECTRON EXCITATION

In order to suppress the hot electron population above the barrier, we have modified the design of the QCC

structure. Instead of using two 6-nm-thick  $\text{Al}_{0.35}\text{Ga}_{0.65}\text{As}$  barriers, as in QCC-A, we replaced them with two 3-nm-thick  $\text{Al}_{0.7}\text{Ga}_{0.3}\text{As}$  barriers in the modified structure [referred to as QCC-B, see Fig. 4(a)]. We made the tunneling probabilities of QCC-B similar to those in QCC-A by keeping the same product of the barrier height and thickness. Temperature-dependent  $I$ - $V$  characteristics of QCC-B are plotted in Fig. 4(b). The resonant tunneling takes place at  $V \sim 0.3 \text{ V}$ . The alignment between  $E_2$  and  $E_1$  and the emitter conduction band edge is expected to occur at  $V \sim 0.7 \text{ V}$  and  $\sim 1.3 \text{ V}$ , respectively, which shows small troughs around these bias voltages due to a shutoff of the resonant tunneling from the emitter conduction band.

Figure 5(a) plots the PL spectra of QCC-B using a log scale measured for various  $V$  at 300 K. The PL intensities from both QWs increase by  $\sim 100$  times when a positive voltage is applied. Figure 5(b) shows the PL peak intensities from the two QWs as a function of  $V$ . We observe a significant increase in the PL intensities from

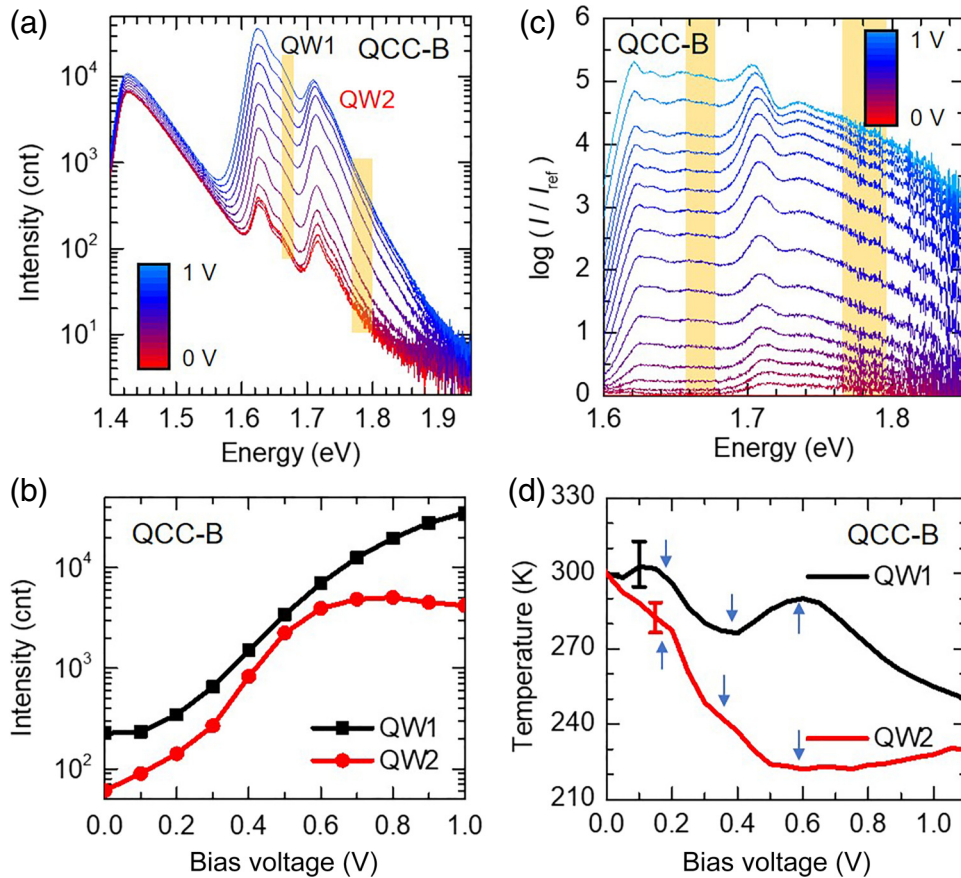


FIG. 5. (a) Photoluminescence (PL) spectra of QCC-B measured at 300 K for various bias voltages. The observed three PL peaks correspond to the radiative recombination of electrons in the electrode ( $\sim 1.43 \text{ eV}$ ) and in the quantum wells (QW1  $\sim 1.62 \text{ eV}$  and QW2  $\sim 1.71 \text{ eV}$ ). The energy ranges of the high-energy tails used for determining the electron temperatures are highlighted in orange. (b) Intensity of the PL peak from QW1 and QW2 as a function of the bias voltage. (c) Ratio between PL spectra measured for various  $V$  and the PL spectrum measured at  $V=0$  for determination of electron temperatures. The energy ranges of high-energy tails are highlighted in orange. (d) Electron temperature of QW1 (black) and QW2 (red) as a function of  $V$ . Blue arrows indicate the positions of the troughs and peaks observed in the electron temperatures.

both QWs with increasing  $V$ , particularly for  $V > 0.3$  V. The two PL intensities gradually approach one another at  $V = 0.5$  V. The PL intensity of QW2 increases until  $V$  reaches 0.8 V and then starts decreasing, suggesting that  $E_2$  drops below  $E_1$ .

In Fig. 5(c), we calculate the ratios between the PL spectra measured at various  $V$  and the reference PL measured at  $V = 0$ , as we did for Fig. 2(c). Figure 5(d) plots the electron temperatures in QW1 (black) and QW2 (red) versus  $V$ . The energy range in the high-energy tail of the QW1 PL spectra for determining  $T_e$  was rather limited (from 1.665 eV to 1.68 eV). The magnitude of ambiguities in the determined  $T_e$  is shown by an error bar in Fig. 5(d) [22]. As seen in Fig. 5(d), when a bias voltage is applied, electron cooling is observed in both QWs. This finding supports our interpretation that the electron heating observed in QW2 of QCC-A [Fig. 2(d)] results from the hot electron population above the collector barrier. Electrons in QW2 are more significantly cooled by thermionic emission by as much as 70 K.

Furthermore, when we examine  $T_e$  in QW1 more carefully, an oscillatory behavior in  $T_e$  is observed as  $V$  is varied. Simultaneously, QW2 also shows weaker oscillatory modulation in  $T_e$ , whose phase is approximately opposite to that of QW1. Since the energy separation between  $E_1$  and  $E_2$  is  $\sim 60$  meV at  $V = 0$  V,  $E_2 - E_1$  is approximately equal to one LO-phonon energy in GaAs (36 meV) when  $V \sim 0.2$  V. At  $V \sim 0.4$  V, the energy separation becomes approximately half of the LO-phonon energy. Moreover,  $T_e$  in QW1 shows a trough at  $V = 0.4$  V and a peak at around  $V \sim 0.6$  V, while  $T_e$  in QW2 reaches a minimum. Next, we discuss the relationship between the oscillations in  $T_e$  and the energy separation between  $E_1$  and  $E_2$ .

In Figs. 6(a)–6(c), we plot the in-plane dispersions of the two-dimensional subbands in QW1 and QW2 when  $\Delta E$  is approximately equal to  $\hbar\omega_{LO}$ ,  $1/2\hbar\omega_{LO}$ , and zero, respectively. Transport from the emitter to QW1 is described by resonant tunneling injection. Transitions from QW1 to QW2 are described by resonant tunneling ( $\sim T(\Delta E)$ ), LO-phonon scattering ( $\sim S_o(\Delta k)$ ), and elastic scattering ( $\sim S_e(\Delta k)$ ), including acoustic phonon and interface roughness scattering. Here,  $\Delta k$  is the in-plane momentum change in the transition. When electron transport from QW1 to QW2 is governed by  $\Delta k = 0$  processes, such as vertical-LO-phonon scattering [Fig. 6(a)] or resonant tunneling [Fig. 6(c)], both input and output powers have no  $k$ -selectivities and  $\Delta P_{QW1}$  equals to zero (for more details, see Appendix B). As a result, no electron cooling or heating is expected in QW1. Concerning QW2,  $\Delta P_{QW2}$  is negative due to thermionic emission and the electron temperature is reduced. When  $V \sim 0.4$  V ( $E_2 - E_1 = \sim 1/2\hbar\omega_{LO}$ ), as shown in Fig. 6(b), LO-phonon-assisted transition from QW1 to QW2 becomes nonvertical and elastic scattering processes also become significant. High kinetic energy electrons in QW1 are preferentially extracted by elastic scattering and  $\Delta P_{QW1}$  becomes negative. After rethermalization, QW1 is cooled. On the other hand, QW2 is cooled by thermionic emission and heated by electron injection from QW1. The anticorrelated oscillatory behavior of  $T_e$  in QW2 is much weaker.

So far, we have discussed the cooling and heating behavior of electrons in successive QWs. However, the cooling mechanism for the lattice is different. We should emphasize that the optimal sequential thermionic emission for lattice cooling is achieved when the successive quantized energy separation is equal to  $\hbar\omega_{LO}$ . Electrons can

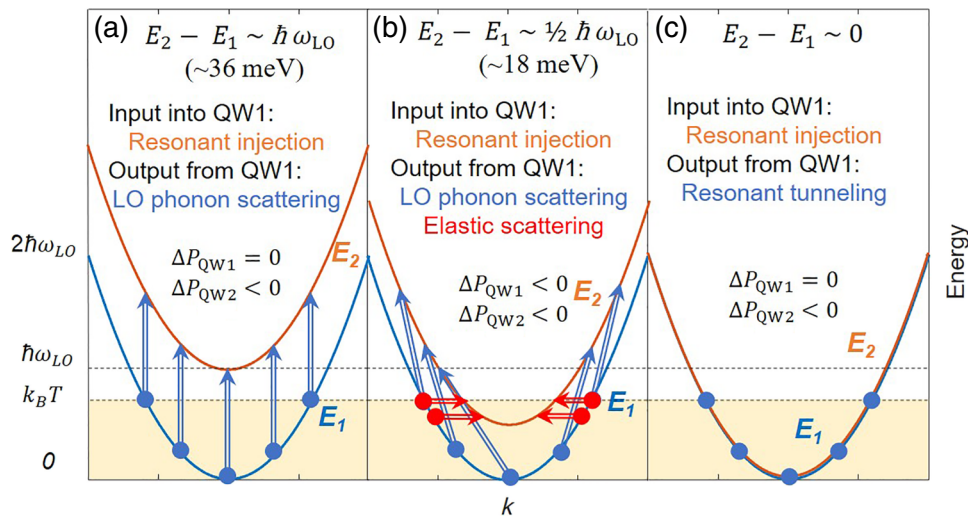


FIG. 6. In-plane dispersions of the two-dimensional subbands in QW1 ( $E_1$ , blue) and QW2 ( $E_2$ , orange) when the energy separation between subbands is approximately (a) 36 meV, (b) 18 meV, and (c) 0 meV, which correspond to the voltages shown by the blue arrows in Fig. 5(d), respectively. Resonant injection into QW1 and the tunneling and scattering processes from QW1 are plotted.

efficiently travel through the successive QW structure by absorbing one LO phonon at each step. Since we cannot determine the lattice temperature in each nanometer-thick QW at present, we cannot provide experimental data for the lattice cooling effect. However, the present observation of electron cooling behavior, which is consistent with our expectation, supports the idea of sequential cascading thermionic cooling.

## VI. SUMMARY AND OUTLOOK

We have investigated evaporative electron cooling in semiconductor cascading double QW structures, in which one electron successively absorbs multiple LO phonons as it travels from the cathode to the anode. By using the high-energy tail of photoluminescence spectra from the two QWs, the electron temperature in each QWs is determined. By introducing taller barriers ( $\text{Al}_{0.7}\text{Ga}_{0.3}\text{As}$ ) before the last QW to suppress hot electron distribution above the barrier, electron cooling in both QWs by several tens of kelvins has been achieved. Furthermore, an anticorrelated oscillation in the electron temperatures in QW1 and QW2 is observed, which is due to an interplay between LO-phonon-assisted tunneling and elastic scattering processes. The reduction in the electron temperature in the second QW was as large as 70 K, which is much larger than that in the asymmetric double barrier structure (typically 30 K) and is likely due to lower electron density in QW2.

In our recent numerical work on the performance of the QCC structure using NEGF calculations [26], we compared the cooling capabilities of the ADB structure with that of the QCC structure and showed that the QCC outperforms the ADB both in the coefficient of performance (COP) and in the cooling power, when the two structures have similar activation energies for the thermionic emission process. The COPs of the ADB/QCC structures lie in the range of  $\sim 10\%$  [26]. The selective energy filtering effect of the resonant tunneling is crucial for achieving such a high efficiency. It has also been reported that this energy filtering effect can make the efficiency of heat engines become close to the thermodynamic limit [27].

Since the final goal of our thermionic cooling structures is to cool the lattice system, the first task is to develop a method to characterize the lattice temperature in nanometer-thick regions. The second task is to enhance the cooling power. Due to small electron densities in  $n$ -type GaAs, the lattice cooling effect of our current structures may be in the microkelvin range [14–16]. One possibility to enhance the lattice cooling power is to increase the number of QW stages in the sequential transition. Another possibility is to dope the structure much more heavily to enhance the current density and improve the balance of the heat capacity of the electron and the lattice systems. For example, it is possible to dope GaAs with acceptors much more heavily (up to a  $10^{21} \text{ cm}^{-3}$  level) than with donors.

Such an effort will lead to future semiconductor-based high-efficiency solid-state cooling technology.

## ACKNOWLEDGMENTS

We thank Daniel Suchet, Thomas Vezin, Fabienne Michelini, and Nicolas Cavassilas for their fruitful discussions. This work has been supported by KAKENHI from JSPS (Grants No. JP19K21957 and No. JPJSCCA20190006) and by the GELATO ANR project (Grant No. ANR-21-CE50-0017).

## APPENDIX A

For nondegenerate electrons and holes in a QW, such as in our case, the intensity of PL from a QW ( $I_{\text{QW}}$ ) follows two-dimensional densities of states [28], i.e.,

$$I_{\text{QW}} \propto Y(h\nu - E_0) \exp\left(-\frac{h\nu - E_0}{k_B T^*}\right), \quad (\text{A1})$$

$$Y(h\nu - E_0) \rightarrow \frac{1}{\pi} \left\{ \frac{\pi}{2} + \arctan\left[\frac{h\nu - E_0}{\Gamma_n}\right] \right\},$$

where  $Y(h\nu - E_0)$  is a step function with a broadening parameter  $\Gamma_n$ . Moreover,  $T^*$  is the effective carrier temperature determined from the high-energy tail of the photoluminescence spectra, which can be expressed via

$$\frac{1}{k_B T^*} = \frac{1}{k_B T_e} \frac{m_v}{m_c + m_v} + \frac{1}{k_B T_h} \frac{m_c}{m_c + m_v}, \quad (\text{A2})$$

$$T^* \approx T_e \left( 1 + \frac{(T_h - T_e)}{T_e} \frac{m_c}{(m_c + m_v)} \right).$$

Here,  $T_e$  and  $T_h$  are the electron and hole temperatures, respectively. In addition,  $m_c$  and  $m_v$  denote the in-plane effective masses of electrons and holes, respectively, and  $m_0$  is the free electron mass. In the present work, we used  $m_c = 0.067m_0$  and  $m_v = 0.09m_0$  for both the  $\text{Al}_{0.1}\text{Ga}_{0.9}\text{As}$  QW (QW1) and the  $\text{Al}_{0.2}\text{Ga}_{0.8}\text{As}$  QW (QW2).

If we assume  $T_h = T_e$  [20],  $T^*$  becomes equal to  $T_e$ . This assumption may be valid since carrier-carrier interaction is, in general, strong except for the fact that there are very few carriers. However, if we assume that the hole temperature is close to the lattice temperature ( $\sim 300$  K) [29,30],  $T_e$  becomes  $\sim 170$  K when  $T^*$  is  $\sim 230$  K. Although we do not know the exact hole temperature, we may have a situation close to  $T_h = T_e$ , owing to efficient carrier-carrier thermalization [20].



## APPENDIX B

The resonant injection current from the emitter to QW1 is expressed as follows [31]:

$$\begin{aligned} J_{\text{in}}(\mu_{\text{QW1}}) &= -\frac{em^*}{2\pi^2\hbar^3} \iint A(\varepsilon_z)\Gamma(E_1)(f(\varepsilon_{fe}) \\ &\quad - f(\mu_{\text{QW1}}))d\varepsilon_{xy}d\varepsilon_z, \\ &= -\frac{em^*\Gamma(E_1)}{\pi\hbar^3} \int_0^\infty f(\varepsilon_{fe}) - f(\mu_{\text{QW1}}) d\varepsilon_{xy}. \end{aligned} \quad (\text{B1})$$

Here,  $\Gamma(E_1)$  is the tunneling rate and  $A(\varepsilon_z)$  expresses the level broadening. The electrons above  $E_1$  are injected into QW1 by resonant tunneling.

The input power from the emitter to QW1 is expressed as

$$\begin{aligned} P_{\text{in}}(\mu_{\text{QW1}}) &= \frac{m^*}{2\pi^2\hbar^3} \iint \varepsilon_k A(\varepsilon_z)\Gamma(E_1)(f(\varepsilon_{fe}) \\ &\quad - f(\mu_{\text{QW1}}))d\varepsilon_{xy}d\varepsilon_z, \\ &= \frac{m^*\Gamma(E_1)}{\pi\hbar^3} \int_0^\infty (E_1 + \varepsilon_{xy})(f(\varepsilon_{fe}) \\ &\quad - f(\mu_{\text{QW1}})) d\varepsilon_{xy}. \end{aligned} \quad (\text{B2})$$

Assuming, for simplicity, a Boltzmann distribution for electrons characterized by a uniform temperature  $T$ , we obtain

$$\begin{aligned} J_{\text{in}}(\mu_{\text{QW1}}) &= -\frac{em^*k_B T}{\pi\hbar^3} \Gamma(E_1) (e^{(-E_1+E_{\text{FE}}/k_B T)} \\ &\quad - e^{(-E_1+\mu_{\text{QW1}}/k_B T)}), \end{aligned} \quad (\text{B3})$$

$$\begin{aligned} P_{\text{in}}(\mu_{\text{QW1}}) &= \frac{m^*k_B T}{\pi\hbar^3} \Gamma(E_1)(E_1 + k_B T) (e^{(-E_1+E_{\text{FE}}/k_B T)} \\ &\quad - e^{(-E_1+\mu_{\text{QW1}}/k_B T)}), \\ &= \frac{E_1 + k_B T}{-e} J_{\text{in}}(\mu_{\text{QW1}}). \end{aligned} \quad (\text{B4})$$

The output current from QW1 to QW2 is expressed by combining the resonant tunneling between the QWs ( $\sim T(\Delta E)$ ), LO-phonon scattering ( $\sim S_o(\Delta k)$ ), and elastic scattering ( $\sim S_e(\Delta k)$ ) so that

$$\begin{aligned} J_{\text{out}}(\mu_{\text{QW1}}, \mu_{\text{QW2}}) &= -\frac{em^*}{\pi\hbar^2} \int_{E_1}^\infty T(\Delta E)(f(\mu_{\text{QW1}}) - f(\mu_{\text{QW2}})) d\varepsilon_{xy} \\ &\quad - \frac{em^*}{\pi\hbar^2} \int_{E_1}^\infty S_o(\Delta k)(f(\mu_{\text{QW1}}) - f(\mu_{\text{QW2}})) d\varepsilon_{xy} \\ &\quad - \frac{em^*}{\pi\hbar^2} \int_{E_2}^\infty S_e(\Delta k)(f(\mu_{\text{QW1}}) - f(\mu_{\text{QW2}})) d\varepsilon_{xy}, \end{aligned} \quad (\text{B5})$$

$$\begin{aligned} P_{\text{out}}(\mu_{\text{QW1}}, \mu_{\text{QW2}}) &= \frac{m^*}{\pi\hbar^2} \int_{E_1}^\infty \varepsilon_k T(\Delta E)(f(\mu_{\text{QW1}}) - f(\mu_{\text{QW2}})) d\varepsilon_{xy} \\ &\quad + \frac{m^*}{\pi\hbar^2} \int_{E_1}^\infty \varepsilon_k S_o(\Delta k)(f(\mu_{\text{QW1}}) - f(\mu_{\text{QW2}})) d\varepsilon_{xy} \\ &\quad + \frac{m^*}{\pi\hbar^2} \int_{E_2}^\infty \varepsilon_k S_e(\Delta k)(f(\mu_{\text{QW1}}) - f(\mu_{\text{QW2}})) d\varepsilon_{xy}. \end{aligned} \quad (\text{B6})$$

Here,  $\Delta E$  is the energy difference between  $E_1$  and  $E_2$  and  $\Delta k$  is the difference between the in-plane electron wavevectors in either well. The input current  $J_{\text{in}}$  is always equal to the output current  $J_{\text{out}}$  due to current continuity. Meanwhile, the major transition of the output component depends on the relative position between  $E_1$  and  $E_2$ . Resonant tunneling and LO-phonon scattering occur when  $\varepsilon_k > E_1$ , while the elastic scattering process becomes possible when  $\varepsilon_k > E_2$ .

(1) When  $E_2 - E_1 = \hbar\omega_{\text{LO}}$ , the output component is dominated by efficient vertical-LO-phonon scattering because the electron-LO-phonon interaction is predominantly due to the Fröhlich type, as a result

$$J_{\text{out}}(\mu_{\text{QW1}}, \mu_{\text{QW2}}) = -A_o \int_0^\infty f(\mu_{\text{QW1}}) - f(\mu_{\text{QW2}}) d\varepsilon_{xy}, \quad (\text{B7})$$

$$\begin{aligned} P_{\text{out}}(\mu_{\text{QW1}}, \mu_{\text{QW2}}) &= \frac{A_o}{e} \int_0^\infty (E_1 + \varepsilon_{xy})(f(\mu_{\text{QW1}}) - f(\mu_{\text{QW2}})) d\varepsilon_{xy}. \end{aligned} \quad (\text{B8})$$

Here,  $A_o \equiv (em^*/\pi\hbar^2)S_o(0)$ . Assuming a Boltzmann distribution characterized by the same temperature  $T$  for QW1 and QW2 for simplicity, we obtain

$$J_{\text{out}}(\mu_{\text{QW1}}, \mu_{\text{QW2}}) = -A_o(e^{(-E_1+\mu_{\text{QW1}}/k_B T)} - e^{(-E_1+\mu_{\text{QW2}}/k_B T)}), \quad (\text{B9})$$

$$\begin{aligned} P_{\text{out}}(\mu_{\text{QW1}}, \mu_{\text{QW2}}) &= \frac{A_o}{e} (E_1 + k_B T)(e^{(-E_1+\mu_{\text{QW1}}/k_B T)} - e^{(-E_1+\mu_{\text{QW2}}/k_B T)}), \\ &= \frac{E_1 + k_B T}{-e} J_{\text{out}}(\mu_{\text{QW1}}, \mu_{\text{QW2}}). \end{aligned} \quad (\text{B10})$$

The current continuity condition requires  $J_{\text{in}}(\mu_{\text{QW1}}) = J_{\text{out}}(\mu_{\text{QW1}}, \mu_{\text{QW2}})$ . Therefore, we obtain  $P_{\text{in}}(\mu_{\text{QW1}}) = P_{\text{out}}(\mu_{\text{QW1}}, \mu_{\text{QW2}})$  and no cooling occurs in QW1.

(1) When  $E_2 - E_1 \approx (1/2)\hbar\omega_{LO}$ , the output component is dominated by nonvertical-LO-phonon-assisted scattering and elastic scattering so that

$$J_{\text{out}}(\mu_{\text{QW1}}, \mu_{\text{QW2}}) = -\frac{em^*}{\pi\hbar^2} \int_0^\infty S_o(\Delta k)(f(\mu_{\text{QW1}}) - f(\mu_{\text{QW2}})) d\varepsilon_{xy} - \frac{em^*}{\pi\hbar^2} \int_0^\infty S_e(\Delta k)(f(\mu_{\text{QW1}}) - f(\mu_{\text{QW2}})) d\varepsilon_{xy}, \quad (\text{B11})$$

$$P_{\text{out}}(\mu_{\text{QW1}}, \mu_{\text{QW2}}) = \frac{m^*}{\pi\hbar^2} \int_0^\infty (E_1 + \varepsilon_{xy})S_o(\Delta k)(f(\mu_{\text{QW1}}) - f(\mu_{\text{QW2}})) d\varepsilon_{xy} + \frac{m^*}{\pi\hbar^2} \int_0^\infty (E_2 + \varepsilon_{xy})S_e(\Delta k)(f(\mu_{\text{QW1}}) - f(\mu_{\text{QW2}})) d\varepsilon_{xy}. \quad (\text{B12})$$

Although  $S_o(\Delta k)$  and  $S_e(\Delta k)$  are energy-dependent, we approximately obtain the following:

$$P_{\text{in}}(\mu_{\text{QW1}}) = \frac{E_1 + k_B T}{-e} J_{\text{in}}(\mu_{\text{QW1}}) = \frac{E_1 + k_B T}{-e} J_{\text{out}}(\mu_{\text{QW1}}, \mu_{\text{QW2}}), \approx \frac{m^*}{\pi\hbar^2} \int_0^\infty (E_1 + \varepsilon_{xy})S_o(\Delta k)(f(\mu_{\text{QW1}}) - f(\mu_{\text{QW2}})) d\varepsilon_{xy} + \frac{m^*}{\pi\hbar^2} \int_0^\infty (E_1 + \varepsilon_{xy})S_e(\Delta k)(f(\mu_{\text{QW1}}) - f(\mu_{\text{QW2}})) d\varepsilon_{xy}. \quad (\text{B13})$$

Note that elastic scattering removes high-energy electrons above  $E_2$  from QW1. Therefore, we have  $P_{\text{out}}(\mu_{\text{QW1}}, \mu_{\text{QW2}}) > P_{\text{in}}(\mu_{\text{QW1}})$ , leading to the cooling of the electrons in QW1.

(1) When  $E_2 - E_1 = 0$ , similarly we find

$$J_{\text{out}}(\mu_{\text{QW1}}, \mu_{\text{QW2}}) = -A_T \int_0^\infty f(\mu_{\text{QW1}}) - f(\mu_{\text{QW2}}) d\varepsilon_{xy}, = -A_T (e^{(-E_1 + \mu_{\text{QW1}}/k_B T)} - e^{-E_1 + \mu_{\text{QW2}}/k_B T}), \quad (\text{B14})$$

$$P_{\text{out}}(\mu_{\text{QW1}}, \mu_{\text{QW2}}) = \frac{A_T}{e} \int_0^\infty (E_1 + \varepsilon_{xy})(f(\mu_{\text{QW1}}) - f(\mu_{\text{QW2}})) d\varepsilon_{xy}, = \frac{A_T}{e} (E_1 + k_B T) (e^{(-E_1 + \mu_{\text{QW1}}/k_B T)} - e^{(-E_1 + \mu_{\text{QW2}}/k_B T)}), = \frac{E_1 + k_B T}{-e} J_{\text{out}}(\mu_{\text{QW1}}, \mu_{\text{QW2}}). \quad (\text{B15})$$

Here,  $A_T \equiv (em^*/\pi\hbar^2)T(0)$ . Finally, we obtain  $P_{\text{in}}(\mu_{\text{QW1}}) = P_{\text{out}}(\mu_{\text{QW1}}, \mu_{\text{QW2}})$  and electron cooling vanishes in QW1.

- 
- [1] G. Pennelli, Review of nanostructured devices for thermoelectric applications, *Beilstein J. Nanotechnol.* **5**, 1268 (2014).  
 [2] J. O. Sofo and G. D. Mahan, Optimum bandgap of a thermoelectric material, *Phys. Rev. B* **49**, 4565 (1994).  
 [3] M. M. Leivo, J. P. Pekola, and D. V. Averin, Efficient Peltier refrigeration by a pair of normal metal/insulator/superconductor junctions, *Appl. Phys. Lett.* **68**, 1996 (1996).  
 [4] G. D. Mahan and L. M. Woods, Multilayer thermionic refrigeration, *Phys. Rev. Lett.* **80**, 4016 (1998).

- [5] A. Ziabari, M. Zebarjadi, D. Vashaee, and A. Shakouri, Nanoscale solid-state cooling: a review, *Rep. Prog. Phys.* **79**, 095901 (2016).  
 [6] A. Shakouri, E. Y. Lee, D. L. Smith, V. Narayanamurti, and J. E. Bowers, Thermoelectric effects in submicron heterostructure barriers, *Microscale Thermophys. Eng.* **2**, 37 (1998).  
 [7] A. Shakouri and J. E. Bowers, Heterostructure integrated thermionic coolers, *Appl. Phys. Lett.* **71**, 1234 (1997).  
 [8] G. D. Mahan, J. O. Sofo, and M. Bartkowiak, Multilayer thermionic refrigerator and generator, *J. Appl. Phys.* **83**, 4683 (1998).

- [9] E. Mykkänen, J. S. Lehtinen, L. Grönberg, A. Shep-  
etov, A. V. Timofeev, D. Gunnarsson, A. Kemppinen, A. J.  
Manninen, and M. Prunnila, Thermionic junction devices  
utilizing phonon blocking, *Sci. Adv.* **6**, eaax9191 (2020).
- [10] G. D. Mahan, Thermionic refrigeration, *J. Appl. Phys.* **76**,  
4362 (1994).
- [11] K. A. Chao, M. Larsson, and A. G. Mal'shukov, Room-  
temperature semiconductor heterostructure refrigeration,  
*Appl. Phys. Lett.* **87**, 022103 (2005).
- [12] A. Yangui, M. Bescond, T. Yan, N. Nagai, and K. Hirakawa,  
Evaporative electron cooling in asymmetric double barrier  
semiconductor heterostructures, *Nat. Commun.* **10**, 4504  
(2019).
- [13] X. Zhu, M. Bescond, T. Onoue, G. Bastard, F. Carosella,  
R. Ferreira, N. Nagai, and K. Hirakawa, Electron trans-  
port in double-barrier semiconductor heterostructures for  
thermionic cooling, *Phys. Rev. Appl.* **16**, 064017 (2021).
- [14] M. Bescond, D. Logoteta, F. Michelini, N. Cavassilas,  
T. Yan, A. Yangui, M. Lannoo, and K. Hirakawa,  
Thermionic cooling devices based on resonant-tunneling  
AlGaAs/GaAs heterostructure, *J. Phys.: Condens. Matter*  
**30**, 064005 (2018).
- [15] M. Bescond and K. Hirakawa, High-performance thermi-  
onic cooling devices based on tilted-barrier, *Phys. Rev.*  
*Appl.* **14**, 064022 (2020).
- [16] M. Bescond, G. Dangoisse, X. Zhu, C. Salhani, and K.  
Hirakawa, Comprehensive analysis of electron evaporative  
cooling in double-barrier semiconductor heterostructures,  
*Phys. Rev. Appl.* **17**, 014001 (2022).
- [17] T. Mano, H. T. Miyazaki, T. Kasaya, T. Noda, and  
Y. Sakuma, Double-sided nonalloyed ohmic contacts to  
Si-doped GaAs for plasmoelectronic devices, *ACS Omega*  
**4** (4), 7300 (2019).
- [18] N. Braslau, Alloyed ohmic contacts to GaAs, *J. Vac. Sci.*  
*Technol.* **19**, 803 (1981).
- [19] M. Ogawa, Alloying behavior of Ni/Au-Ge films on GaAs,  
*J. Appl. Phys.* **51**, 406 (1980).
- [20] J. Shah and R. Leite, Radiative recombination from pho-  
toexcited hot carriers in GaAs, *Phys. Rev. Lett.* **22**, 1304  
(1969).
- [21] G. Lasher and F. Stern, Spontaneous and stimulated recom-  
bination radiation in semiconductors, *Phys. Rev.* **133**, A553  
(1964).
- [22] See Supplementary Information at <http://link.aps.org/supplemental/10.1103/PhysRevApplied.22.034012> for experi-  
mental details.
- [23] PL measurements were performed through a semitranspar-  
ent NiCr window fabricated inside the AuNiGe contact  
region on the top of the mesa structures to make the elec-  
tric field across the mesa region as uniform as possible.  
However, since the contact between the NiCr film and  
the heavily doped GaAs contact layer is not ohmic, we  
have a residual series resistance effect. As a result, we  
observe resonance between E1 and E2 at  $V \sim 0.3$  V in the  
transport measurements at 6 K (see Fig. 1), while the reso-  
nance occurs at  $V \sim 0.6$  V in the optical characterization at  
300 K (see Fig. 2). Measurements at 300 K may shift the  
resonance voltage to a slightly larger voltage than at 6 K.
- [24] H. Esmailpour, L. Lombez, M. Giteau, A. Delamarre, D.  
Ory, A. Cattoni, S. Collin, J.-F. Guillemoles, and D. Suchet,  
Investigation of the spatial distribution of hot carriers in  
quantum-well structures via hyperspectral luminescence  
imaging, *J. Appl. Phys.* **128**, 165704 (2020).
- [25] A. Philippe, F. Carosella, X. Zhu, C. Salhani, K. Hirakawa,  
M. Bescond, R. Ferreira, and G. Bastard, Rate equations  
description of the asymmetric double barrier electronic  
cooler, *J. Appl. Phys.* **134**, 124305 (2023).
- [26] G. Etesse, C. Salhani, X. Zhu, N. Cavassilas, K. Hirakawa,  
and M. Bescond, Selective energy filtering in a multiple-  
quantum-well nanodevice: The quantum cascade cooler,  
*Phys. Rev. Appl.* **21**, 054010 (2024).
- [27] Martin Josefsson, Artis Svilans, Adam M. Burke, Eric A.  
Hoffmann, Sofia Fahlvik, Claes Thelander, Martin Lei-  
jnse, and Heiner Linke, A quantum-dot heat engine oper-  
ating close to the thermodynamic efficiency limits, *Nat.*  
*Nanotechnol.* **13**, 920 (2018).
- [28] G. Bastard, *Wave Mechanics Applied to Semiconductor*  
*Heterostructures* (Editions de Physique, Les Ulis, France,  
1990), pp. 281–284.
- [29] J. Shah, Hot carriers in quasi-2-D polar semiconductors,  
*IEEE J. Quantum Electron.* **22** (9), 1728 (1986).
- [30] R. A. Höpfel, J. Shah, and A. C. Gossard, Nonequilibrium  
electron-hole plasma in GaAs quantum wells, *Phys. Rev.*  
*Lett.* **56**, 765 (1986).
- [31] S. Datta, *Quantum Transport: Atom to Transistor* (Cam-  
bridge University Press, New York, 2005).